

## Four-wave-cooling to the single phonon level in Kerr optomechanics

Daniel Bothner <sup>1,2,3</sup>✉, Ines C. Rodrigues <sup>1,3</sup> & Gary A. Steele <sup>1</sup>✉

Cavity optomechanics has achieved groundbreaking control and detection of mechanical oscillators, based on their coupling to linear electromagnetic modes. Recently, however, there is increasing interest in cavity nonlinearities as resource in radiation-pressure interacting systems. Here, we present a flux-mediated optomechanical device combining a nonlinear superconducting quantum interference cavity with a mechanical nanobeam. We demonstrate how the Kerr nonlinearity of the circuit can be used to enhance the device performance by suppressing cavity frequency noise, and for a counter-intuitive sideband-cooling scheme based on intracavity four-wave-mixing. With a large single-photon coupling rate of up to  $g_0 = 2\pi \cdot 3.6$  kHz and a high mechanical quality factor  $Q_m \approx 4 \cdot 10^5$ , we achieve an effective four-wave cooperativity of  $C_{\text{fw}} > 100$  and demonstrate four-wave cooling of the mechanical oscillator close to its quantum groundstate. Our results advance the recently developed platform of flux-mediated optomechanics and demonstrate how cavity Kerr nonlinearities can be utilized in cavity optomechanics.

<sup>1</sup>Kavli Institute of Nanoscience, Delft University of Technology, PO Box 5046, 2600 GA Delft, The Netherlands. <sup>2</sup>Physikalisches Institut, Center for Quantum Science (CQ) and LISA+, Universität Tübingen, Auf der Morgenstelle 14, 72076 Tübingen, Germany. <sup>3</sup>These authors contributed equally: Daniel Bothner and Ines C. Rodrigues. ✉email: [daniel.bothner@uni-tuebingen.de](mailto:daniel.bothner@uni-tuebingen.de); [g.a.steele@tudelft.nl](mailto:g.a.steele@tudelft.nl)

Cavity optomechanical systems are the leading platform for the detection and manipulation of mechanical oscillators with electromagnetic fields from the nano- to the macroscale<sup>1</sup>. Displacement detection with an imprecision below the standard quantum limit<sup>2,3</sup>, sideband cooling to the motional quantum groundstate<sup>4,5</sup>, the preparation of nonclassical states of motion<sup>6–9</sup>, quantum entanglement of distinct mechanical oscillators<sup>10,11</sup>, topological energy transfer using exceptional points<sup>12</sup>, and microwave-to-optical-frequency transducers<sup>13,14</sup> are just some of the highlights that have been reported during the last decade. All of these impressive results have been achieved with linear cavities, linear mechanical oscillators, and in the linearized regime of the optomechanical interaction utilizing large-amplitude cavity control fields, which however limits the available possibilities for mechanical-state detection and control.

Very recently, an exciting scheme to couple a mechanical oscillator to microwave photons in a superconducting LC circuit has been realized: flux-mediated optomechanical coupling<sup>15–18</sup>. In this approach, the displacement of a mechanical oscillator is transduced to magnetic flux threading a superconducting quantum-interference device (SQUID) embedded in a microwave LC circuit as flux-dependent inductance<sup>19–21</sup>. Due to the scaling of the optomechanical single-photon coupling rate  $g_0$  with the external magnetic transduction field in flux-mediated optomechanics<sup>15,21</sup>, record single-photon coupling rates for the microwave domain have been reported<sup>16–18</sup> and achieving the long-sought-after optomechanical single-photon regime<sup>22,23</sup> or even the ultrastrong coupling to superconducting qubits<sup>24</sup> seems feasible in future devices.

Naturally, this platform comes along with its own opportunities and challenges. First, a SQUID constitutes a nonnegligible Kerr nonlinearity, which is typically undesired in optomechanics, as it, for instance, limits the maximally applicable power of a red-sideband cooling tone due to the appearance of an exceptional point and a bifurcation instability in the Kerr cavity susceptibility<sup>25</sup>. Nevertheless, intrinsic nonlinearities and parametrically driven cavities are also potentially promising resources for optomechanical systems and have attracted increasing interest in this context lately<sup>20,26–31</sup>. Second, SQUIDs are extremely flux-sensitive devices and therefore flux-mediated optomechanics is susceptible to flux noise, which can lead to fluctuating-cavity frequencies, an effect unwanted in optomechanical protocols. When dealing with nonlinear systems, frequency fluctuations are particularly challenging as they can cause the cavity to switch unexpectedly across the bifurcation threshold at high driving powers. Developing protocols to work around these challenges is of utmost importance for any optomechanical system composed of noisy cavities and Kerr nonlinearities, and flux-mediated optomechanics is the ideal platform to study these regimes in a highly designable and flexible scenario.

Here, we engineer a flux-mediated optomechanical device with a large single-photon coupling rate of up to  $g_0 \approx 2\pi \cdot 3.6$  kHz and demonstrate sideband cooling of the mechanical oscillator close to its quantum groundstate by intracavity four-wave mixing (4WM). The four-wave cooling scheme we implement here demonstrates how the cavity Kerr nonlinearity itself can be utilized for reducing cavity-frequency noise and for evading the Kerr cavity bifurcation instability in optomechanical sideband cooling. By using a strong parametric cavity drive, we activate the emergence of two Kerr quasi-modes in the SQUID circuit and realize an optomechanical coupling of these quasi-modes to the mechanical oscillator by an additional optomechanical sideband-pump field. The drive-activated Kerr modes show enhanced properties such as a reduced effective linewidth compared with the undriven circuit, and in particular, a suppression of cavity-frequency fluctuations by an internal stabilization-feedback loop. In this scheme, we achieve effective single-photon cooperativities

$C_0 \gtrsim 10$  and strikingly find that blue-detuned optomechanical sideband pumping leads to dynamical backaction with the characteristics of red-sideband pumping in a standard optomechanical system, in particular to positive optical damping. This surprising result is a consequence of sideband interference due to 4WM and allows to evade the Kerr bistability that is only relevant for red-detuned pumping. We finally use this blue-detuned optical damping to cool the mechanical oscillator to a residual occupation of  $n_m \sim 1.6$ . Our results demonstrate how cavity Kerr nonlinearities can be used in optomechanics to achieve both, enhanced device performance and unexplored control schemes for mechanical oscillators. At the same time, they reveal the potential of flux-mediated optomechanics regarding low-power groundstate cooling of mechanical oscillators and the future preparation of quantum states of motion.

## Results

**The device.** Our device combines a superconducting quantum-interference LC circuit with a mechanical nanobeam oscillator embedded into the loop of the SQUID, cf. Fig. 1a–c. Details on device fabrication are given in Supplementary Note 1. At the core of the circuit, the SQUID acts as a magnetic-flux-dependent inductance  $L_S(\Phi)$ , where  $\Phi$  is the total magnetic flux threading the  $21 \times 3 \mu\text{m}^2$  large loop. For the tunable optomechanical coupling between the displacement of the mechanical nanobeam and the microwave circuit, two distinct external magnetic fields are required. First, a magnetic field perpendicular to the chip surface  $B_\perp$  is used to change the magnetic-flux bias  $\Phi_\perp$  through the SQUID loop, allowing to tune the circuit resonance frequency  $\omega_0$  and flux responsivity  $\mathcal{F} = \partial\omega_0/\partial\Phi$ . Second, a magnetic in-plane field  $B_\parallel$  is used to transduce the out-of-plane displacement  $\delta x$  of the mechanical oscillator to additional flux  $\Phi_\parallel = B_\parallel l_m \delta x$ , where  $l_m = 18 \mu\text{m}$  is the length of the mechanical beam. To apply these two fields, the chip is mounted into a homemade 2D vector magnet, consisting of a large split coil for  $B_\parallel$  and an additional small coil mounted below the chip for the generation of  $B_\perp$ , cf. Fig. 1d. The whole configuration is placed in a cryoperm magnetic shielding and attached to the mK plate of a dilution refrigerator with a base temperature  $T_b \approx 15$  mK. More details on the measurement setup are given in Supplementary Notes 2 and 3.

We perform the experiments presented here at in-plane fields of  $B_\parallel = 21$  mT and  $B_\parallel = 25$  mT. Figure 1e shows the transmission response of the cavity for  $B_\parallel = 25$  mT and at the bias-flux sweet spot. It has a resonance frequency  $\omega_0 = 2\pi \cdot 5.2673$  GHz, a total linewidth  $\kappa = 2\pi \cdot 380$  kHz, and an external linewidth  $\kappa_e = 2\pi \cdot 110$  kHz. Figure 1f shows how the cavity resonance frequency can be tuned by  $\sim 150$  MHz by changing the applied flux bias  $\Phi_\perp$  threading the SQUID loop. The curves and cavity parameters at  $B_\parallel = 21$  mT only deviate slightly from the ones given here, the corresponding additional data can be found in Supplementary Note 4. Due to an improved SQUID design and fabrication, the cavity-flux responsivity  $\mathcal{F}$  is increased by one order of magnitude compared with our previous results<sup>15</sup>, which leads to a significantly enhanced single-photon coupling rate

$$g_0 = \mathcal{F} B_\parallel l_m x_{zpf} \quad (1)$$

where  $x_{zpf}$  is the mechanical zero-point fluctuation amplitude.

The mechanical nanobeam, visible in Fig. 1b and released from the substrate in an isotropic reactive ion-etching process using SF<sub>6</sub> plasma<sup>32</sup>, is 500 nm wide and 70 nm thick. From its total mass of  $m \approx 1.9$  pg and the resonance frequency of the out-of-plane mode  $\Omega_m \approx 2\pi \cdot 5.32$  MHz, we get  $x_{zpf} = \sqrt{\frac{\hbar}{2m\Omega_m}} \approx 30$  fm. For an in-plane field of  $B_\parallel = 25$  mT, and the two flux-bias points  $\Phi_I$  and  $\Phi_{II}$ , cf. Fig. 1f, we obtain single-photon coupling rates  $g_{0,I} = 2\pi \cdot 1.9$  kHz and  $g_{0,II} = 2\pi \cdot 3.6$  kHz with  $\mathcal{F}_I = 2\pi \cdot 300$  MHz/ $\Phi_0$  and

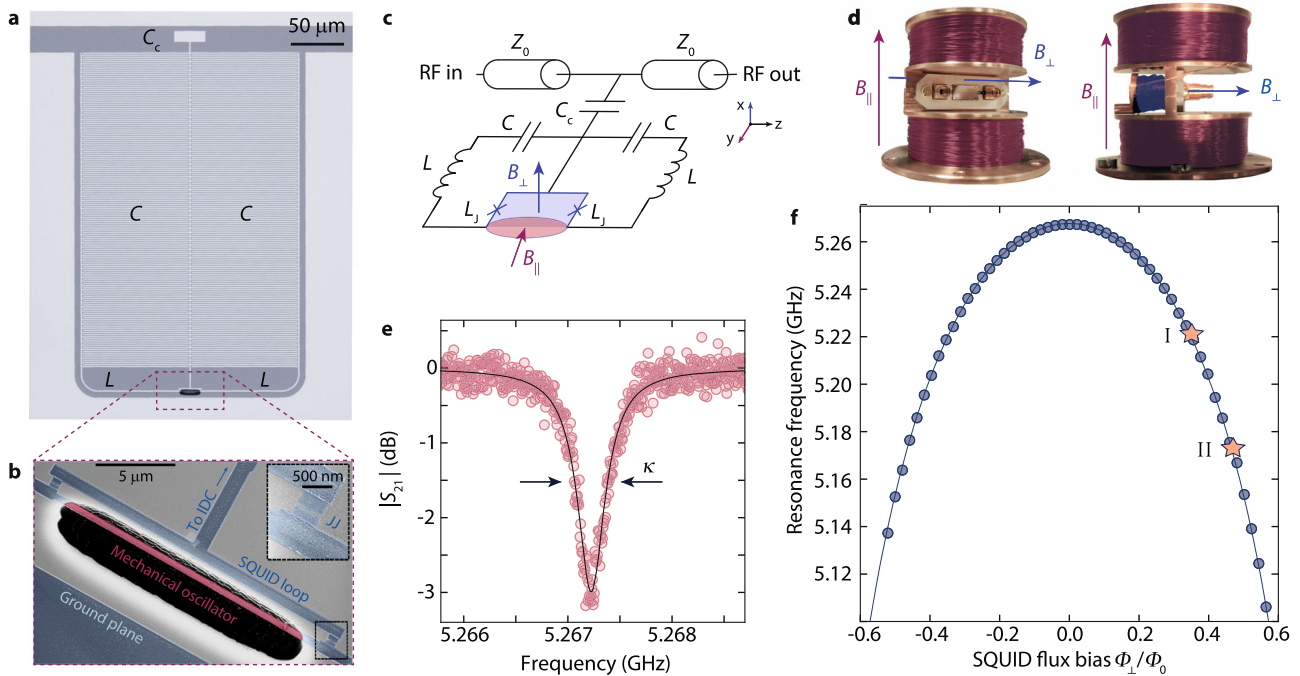


**Fig. 1** A superconducting quantum-interference cavity parametrically coupled to a mechanical nanobeam. **a** Optical micrograph of the circuit. Bright parts are aluminum, dark parts are silicon substrate. The LC circuit combines two interdigitated capacitors (IDCs)  $C$  with two linear inductors  $L$ , connected through a superconducting quantum-interference device (SQUID) with total Josephson inductance  $L_S = L_J/2$ . The circuit is capacitively coupled to a  $Z_0 = 50 \Omega$  coplanar waveguide feedline (top of image) with a coupling capacitor  $C_c$  and surrounded by ground plane. **b** Scanning electron micrograph of the constriction-type SQUID, showing the two Josephson junctions and the mechanical oscillator as part of the loop released from the substrate. The inset shows a zoom-in to one of the nanobridge Josephson junctions. **c** Circuit equivalent of the device. For the experiments, two magnetic fields can be applied. The field  $B_{\perp}$  is oriented perpendicular to the chip plane and is used to set the flux-bias working point of the SQUID  $\Phi_{\perp}$ . The parallel field  $B_{\parallel}$  transduces mechanical displacement of the out-of-plane mode to additional flux  $\Phi_{\parallel} = B_{\parallel} \delta x$  threading the SQUID loop. **d** shows the sample integrated into a printed-circuit board with two microwave connectors and mounted into a 2D vector magnet. The large split coil is used to generate  $B_{\perp}$ , a small single coil behind the chip generates  $B_{\parallel}$ . **e** Transmission response  $|S_{21}|$  of the cavity at  $B_{\parallel} = 25$  mT and  $B_{\perp} = 0$ . From a fit to the data, we extract the resonance frequency  $\omega_0 = 2\pi \cdot 5.2673$  GHz, the total linewidth  $\kappa = 2\pi \cdot 380$  kHz, and the external linewidth  $\kappa_e = 2\pi \cdot 110$  kHz. Data are shown as circles, fit as black line. **f** Resonance frequency  $\omega_0$  vs magnetic flux  $\Phi_{\perp}$ , normalized to one-flux quantum  $\Phi_0$  at  $B_{\parallel} = 25$  mT. Circles are data, line is a fit. The two operation points for this paper are marked with stars and denoted “I” for  $\omega_0 \approx 2\pi \cdot 5.22$  GHz and “II” for  $\omega_0 \approx 2\pi \cdot 5.17$  GHz. Details on measurements and fits can be found in Supplementary Note 4.

$\mathcal{F}_{\text{II}} = 2\pi \cdot 520$  MHz/ $\Phi_0$ . For the smaller in-plane field of  $B_{\parallel} = 21$  mT, the  $g_0$ -values are scaled accordingly, cf. Supplementary Note 5.

The final important parameter of the device is its Kerr nonlinearity, which at the flux sweetspot is  $\mathcal{K}/2\pi = -30$  kHz. For the two flux-bias operation points I and II, we obtain  $\mathcal{K}_I/2\pi = -40$  kHz and  $\mathcal{K}_{\text{II}}/2\pi = -55$  kHz, respectively. More details on the determination of the circuit parameters and their flux dependence can be found in Supplementary Note 4.

**Driven Kerr modes and dynamical Kerr backaction.** Owing to the Kerr anharmonicity  $\mathcal{K}$ , the application of a strong microwave-drive tone close to the cavity resonance frequency  $\omega_0$  significantly modifies the cavity response to an additional probe field. In Fig. 2, we discuss this modified response in the presence of a parametric drive tone with a fixed frequency  $\omega_d$ , when the cavity is tuned to cross this drive tone by means of the bias field  $B_{\perp}$ . For large detunings between cavity and drive, the circuit response  $S_{21}$  exhibits a standard single-mode resonance lineshape. However, as the detuning  $\Delta_d = \omega_d - \omega_0$  is reduced, the driven-cavity susceptibility

$$\chi_g(\Omega) = \frac{\tilde{\chi}_p(\Omega)}{1 - \mathcal{K}^2 n_d^2 \tilde{\chi}_p(\Omega) \tilde{\chi}_p^*(-\Omega)} \quad (2)$$

deviates considerably from a single linear cavity, leading to the

regime of parametric amplification and degenerate four-wave mixing, which is experimentally identified by the appearance of a second mode, cf. Fig. 2a, b. Here,  $\Omega = \omega - \omega_d$  denotes the detuning between the probe field at  $\omega$  and the parametric drive and

$$\tilde{\chi}_p(\Omega) = \frac{1}{\frac{\kappa}{2} + i(\Delta_d - 2\mathcal{K}n_d + \Omega)}. \quad (3)$$

The two Kerr quasi-modes, which we denote as signal and idler resonance, appear symmetrically around the drive with complex resonance frequencies

$$\omega_{i/s} = \omega_d + i\frac{\kappa}{2} \pm \sqrt{(\Delta_d - \mathcal{K}n_d)(\Delta_d - 3\mathcal{K}n_d)} \quad (4)$$

where  $n_d$  is the parametric drive intracavity photon number. These Kerr modes have been observed and discussed also in the context of optical cavities and mechanical oscillators<sup>33–35</sup>. The signal mode can be identified by the shifted and significantly deepened cavity absorption dip and the idler mode by the resonance peak, indicating net transmission gain by Josephson parametric amplification.

With the activation of the quasi-mode state, we obtain a highly stabilized effective resonance frequency and linewidth, while the bare cavity suffers from considerable frequency fluctuations due to flux noise. Due to the reduction of frequency

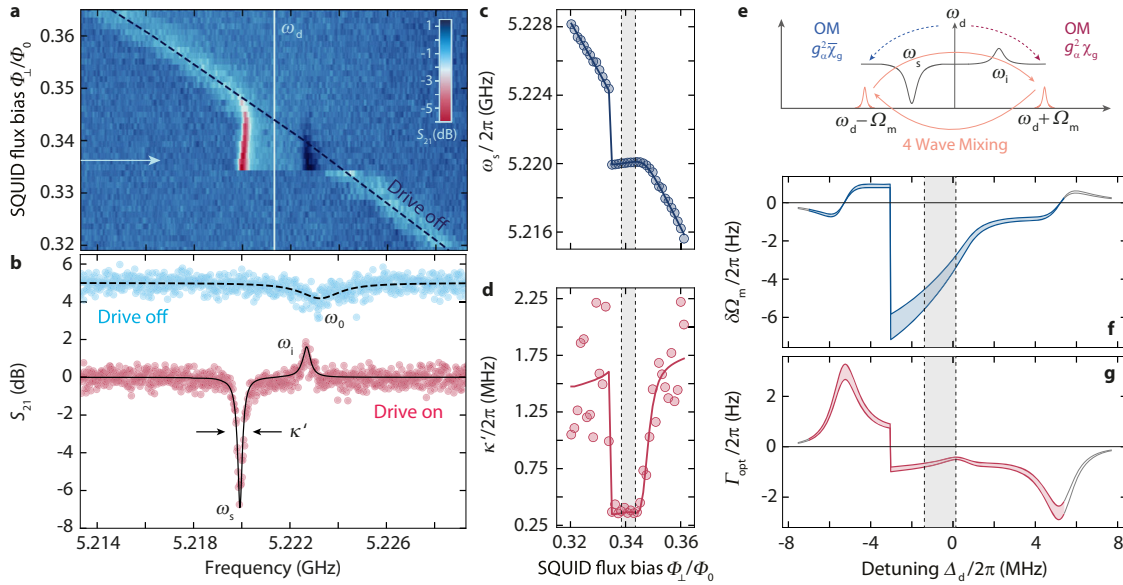


**Fig. 2** Cavity stabilization by activation of the Kerr quasi-mode state and single-tone dynamical Kerr backaction. **a** Color-coded magnitude of the SQUID cavity response  $S_{21}$  vs SQUID flux bias  $\Phi_{\perp}/\Phi_0$  in the presence of a strong drive at  $\omega_d$ . The flux-bias range corresponds to a small variation of  $\Phi_{\perp}$  around operation point I and  $B_{\parallel} = 25$  mT. When the flux-tunable resonance frequency  $\omega_0$ , indicated as dashed line and labeled “Drive off”, is far detuned from the drive tone, the cavity response exhibits a single broad absorption resonance. As the detuning between cavity and drive  $\Delta_d = \omega_d - \omega_0$  is reduced, the cavity response is significantly modified and the original resonance is developing into a double-mode structure. The appearance of these driven Kerr quasi-modes indicates the onset of parametric amplification and degenerate 4WM in the SQUID circuit. We denote the two modes as signal and idler resonance with the resonance frequencies  $\omega_s$  and  $\omega_i$ , respectively. The arrow on the left indicates the position of the linescan shown in panel **b**. In addition to the linescan from **a** (red circles) and the result of the analytical response calculation (solid black line), we show the equivalent linescan without parametric drive (blue circles) and its corresponding theoretical response (dashed black line). The curves without parametric drive are offset by +5 dB for clarity. Panels **c** and **d** show  $\omega_s$  and effective linewidth  $\kappa'$  of the signal resonance vs flux bias. Lines show the result of modeling the effective quantities with the driven Kerr cavity equations and taking into account flux-noise broadening and two-level systems. The stabilized regime of operation is indicated by dashed lines and shaded areas. Here, the linewidth is nearly constant with  $\kappa'/2\pi \approx 340$  kHz. The width of the operation range corresponds to the flux-noise standard deviation, which we estimate to be  $\sigma_{\Phi} \sim 5$  m $\Phi_0$ . Panel **e** illustrates the dynamical Kerr backaction of the drive fields to the nanobeam. Optomechanical (OM) up- and downscattering induces cooling and heating/amplification to the mechanical mode, respectively, where  $g_{\alpha}$  is the multiphoton coupling rate and  $\chi_g$  is the probe-field susceptibility. In addition, interference between up- and downscattered fields due to degenerate 4WM has to be taken into account. **f** and **g** show the calculated optical spring and optical damping. The two blue/red lines and shaded area correspond to  $g_0/2\pi = (1.95 \pm 0.1)$  kHz. The detuning range  $\Delta_d$  is slightly increased compared with **a-d**. In the additional range, the backaction is plotted in gray.

fluctuations in combination with a saturation of two-level system losses by the parametric drive (cf. Supplementary Note 6), the effective cavity linewidth is reduced from the flux-noise broadened  $\kappa'_{\text{off}} \sim 2\pi \cdot 1.5$  MHz to the driven  $\kappa'_{\text{on}} \approx 2\pi \cdot 340$  kHz. An analysis of the signal-mode resonance frequency and linewidth in the presence of the parametric drive is provided in Fig. 2c, d. Within a small region of flux-bias values, the drive-tone-induced Kerr shift compensates for the flux-noise-induced frequency shifts by means of an internal feedback loop. The working principle of this internal feedback is simple: when the bare cavity frequency shifts due to a change in SQUID flux, the intracavity drive-photon number  $n_d$  gets adjusted by this new detuning  $\Delta_d$  between bare cavity and drive. As a consequence, the quasi-mode frequencies, which depend on both  $\Delta_d$  and the Kerr term  $\mathcal{K}n_d$ , cf. Eq. (4), remain nearly constant. Strikingly, this mechanism yields an internal stabilization of the driven resonance and minimizes the impact of flux noise, which thereby becomes the natural choice of operation regime during the following experiments.

In an optomechanical system, any intracavity field also acts back on the mechanical oscillator by altering its resonance frequency and decay rate, an effect known as dynamical backaction<sup>36,37</sup>. Therefore, the effect of the parametric drive to the mechanical oscillator also requires some careful consideration. To model this, we use the linearized equations of motion for

the mechanical amplitude field  $\hat{b}$  and the intracavity fluctuation field  $\hat{a}$  in a single-tone-driven Kerr cavity

$$\dot{\hat{b}} = \left( i\Omega_m - \frac{\Gamma_m}{2} \right) \hat{b} - ig_{\alpha}(\hat{a} + \hat{a}^{\dagger}) + \sqrt{\Gamma_m} \hat{\zeta} \quad (5)$$

$$\begin{aligned} \dot{\hat{a}} = & \left[ -i(\Delta_d - 2\mathcal{K}n_d) - \frac{\kappa}{2} \right] \hat{a} + i\mathcal{K}n_d \hat{a}^{\dagger} \\ & - ig_{\alpha}(\hat{b} + \hat{b}^{\dagger}) + \sqrt{\kappa_i} \hat{\xi}_i + \sqrt{\kappa_e} \hat{\xi}_e \end{aligned} \quad (6)$$

with multiphoton coupling rate  $g_{\alpha} = \sqrt{n_d}g_0$  and input-noise fields  $\hat{\zeta}$ ,  $\hat{\xi}_i$  and  $\hat{\xi}_e$ <sup>1,4</sup>. The input-noise fields describe drive fields related to the thermal and quantum baths of the oscillators, more details can be found in Supplementary Note 7. From the equations of motion, the effective mechanical susceptibility can be derived as

$$\chi_0^{\text{eff}}(\Omega) = \frac{1}{\frac{\Gamma_m}{2} + i(\Omega - \Omega_m) + \Sigma_k(\Omega_m)} \quad (7)$$

for the weak-coupling and high- $Q_m$  limit, which is safely fulfilled for our mechanical oscillator with a linewidth of  $\Gamma_m \approx 2\pi \cdot 13$  Hz. The single-tone dynamical Kerr backaction

$$\Sigma_k(\Omega_m) = g_{\alpha}^2 \left[ \chi_g(1 - \bar{\mathcal{A}}) - \bar{\chi}_g(1 - \mathcal{A}) \right] \quad (8)$$

with  $\chi_g = \chi_g(\Omega_m)$  and  $\bar{\chi}_g = \chi_g^*(-\Omega_m)$  has almost the same form as in linear optomechanics, but with a modified cavity susceptibility  $\chi_g$ . A striking difference, however, is found in the terms  $\mathcal{A} = -i\mathcal{K}n_d\tilde{\chi}_p(\Omega_m)$  and  $\bar{\mathcal{A}} = i\mathcal{K}n_d\tilde{\chi}_p^*(-\Omega_m)$ . These terms correspond to an interference of the red and blue mechanical sideband fields, which occurs due to intracavity four-wave mixing in a driven Kerr cavity. By this 4WM, the two standard mechanical sidebands become idler fields of each other. A schematic of the dynamical backaction and the sideband interference is shown in Fig. 2e.

The optical spring  $\delta\Omega_m = -\text{Im}[\Sigma_k(\Omega_m)]$  and optical damping  $\Gamma_{\text{opt}} = 2\text{Re}[\Sigma_k(\Omega_m)]$  caused by the dynamical Kerr backaction are displayed in Fig. 2f, g. When the drive is located around one mechanical frequency detuned from the cavity  $|\Delta_d| \approx \Omega_m = 2\pi \cdot 5.32$  MHz, the backaction looks very similar to that of a linear cavity. However, when the drive and the cavity are near-resonant, the backaction is strongly dominated by the intracavity photon number and a Duffing-like behavior can be observed with a sudden transition from high- to low-amplitude state at  $\Delta_d \approx -2\pi \cdot 3$  MHz. In the operation regime for the experiments described here, the drive-induced backaction for operation point I is small with  $\Gamma_{\text{opt}}/2\pi \sim -1$  Hz and  $\delta\Omega_m/2\pi \sim -5$  Hz. Using the bare mechanical linewidth  $\Gamma_m \sim 2\pi \cdot 13$  Hz, the corresponding phonon occupation is therefore increased by about 10%, a detailed calculation and discussion of the resulting mechanical-mode occupation is given in Supplementary Note 7.

Due to the considerable cavity flux noise outside of the driven quasi-mode regime, we unfortunately cannot experimentally access the dynamical Kerr backaction for the detuning range shown in Fig. 2. Nevertheless, with a larger single-photon coupling rate  $g_0$  at operation point II and a stronger drive tone, we observe regimes of mechanical instability induced by the dynamical Kerr backaction, which are in excellent agreement with the prediction from the theory. The corresponding data and analysis are explained in detail in Supplementary Note 7. The presented formalism for the dynamical Kerr backaction can also directly be applied to the sideband-unresolved regime and explains the experimental findings of a recent experiment with a similar SQUID cavity optomechanical device<sup>16</sup>, cf. also Supplementary Note 7.

**Multitone dynamical four-wave backaction.** An interesting question arising now is how the Kerr quasi-modes couple to the mechanical nanobeam, when an additional optomechanical pump tone is applied to one of the Kerr-mode sidebands. One might expect that the coupling to the mechanical oscillator is suppressed in this state, similar to the reduced impact of flux noise, as the Kerr-mode frequencies  $\omega_s$  and  $\omega_i$  display only a very weak dependence on flux through the SQUID. Fluctuations of the bare resonance frequency, however, lead to modulations of  $\alpha_d$  and parametric gain, and therefore will impact the mechanical oscillator by inducing changes in the radiation-pressure force. A straightforward way to investigate this setting experimentally is to apply an additional optomechanical pump tone on the red sideband of the signal resonance, i.e., with a pump frequency  $\omega_p \approx \omega_s - \Omega_m$ . Once in this configuration, a weak probe signal around  $\omega \approx \omega_p + \Omega_m$  can be used to detect optomechanically induced transparency (OMIT)<sup>38</sup> and thereby characterize the optomechanical interaction. A detailed theoretical description as well as a discussion of the experimental findings for this red-sideband pumping setup is given in Supplementary Notes 12–15.

A conceptually less straightforward and more exciting possibility is to pump the idler resonance on its blue sideband  $\omega_p \approx \omega_i + \Omega_m$ , cf. Fig. 3a. A blue-detuned pump is commonly associated with amplification/heating due to the favored Stokes scattering to lower-energy photons. The Kerr-mode susceptibility

$\chi_g$  close to the idler resonance, however, resembles that of an “inverted” mode. Any small intracavity field in the driven Kerr cavity experiences in addition a mirroring effect due to degenerate four-wave mixing with the parametric drive tone. The presence of the blue-sideband pump field enriches this situation even further. Then, the Kerr cavity is effectively oscillating with  $\Omega_{\text{dp}} = \omega_d - \omega_p$  due to the presence of two strong fields, and the effects arising from nondegenerate four-wave mixing (cross-mixing) can impact probe fields and mechanical sideband fields and finally also the OMIT response and the backaction to the mechanical oscillator.

A clear signature of the parametric state and four-wave mixing is the appearance of optomechanically induced transparency in the probe response of the signal resonance, when the idler Kerr mode is pumped on its blue sideband. Corresponding data are shown in Fig. 3c, d. Here and in stark contrast to the usual OMIT protocol, the frequency detuning between the idler blue-sideband pump and the probe tone is not even close to the mechanical resonance frequency but given by  $\Omega = \omega - \omega_p \approx 2\Omega_{\text{dp}} + \Omega_m$ . To first order, the observation of this transparency can be understood by considering the intracavity-generated tones in addition to the ones that are sent externally. The parametric drive generates an intracavity field with amplitude  $\alpha_d$  at  $\omega_d$ , and the optomechanical pump at  $\omega_p$  generates an intracavity field with amplitude  $\gamma_-$ . Just by this doubly driven configuration, a third intracavity “pump” field is generated by degenerate 4WM at  $\omega_+ = \omega_p + 2\Omega_{\text{dp}}$  and we denote its amplitude as  $\gamma_+$ . Therefore, when  $\omega_p = \omega_i + \Omega_m$ , the  $\gamma_+$ -field is located at the red sideband of the signal resonance  $\omega_+ = \omega_s - \Omega_m$ . The beating between a probe field at  $\omega \approx \omega_s$  and the  $\gamma_+$ -field is then near-resonant with the mechanical oscillator and will drive it into coherent motion. A second beating component, which is driving the mechanical oscillator, originates from the beating of the  $\gamma_-$ -field and the idler field of the weak probe itself, cf. Fig. 3b. These two are also near-resonant with the mechanical oscillator. Once in coherent motion, the mechanical oscillator generates sidebands to all intracavity-field Fourier components, some of which interfere with the original probe tone, causing the observed appearance of four-wave OMIT.

To characterize the dynamical backaction imprinted by the intracavity fields on the mechanical oscillator in the presence of the  $\alpha_d$ ,  $\gamma_-$ , and  $\gamma_+$  fields, we measure the optomechanical transparency response for varying detuning  $\delta_p$  between the  $\gamma_-$ -field and the idler-mode blue sideband. For each detuning, we determine the effective mechanical resonance frequency  $\Omega_{\text{eff}}$  and effective mechanical linewidth  $\Gamma_{\text{eff}}$  from a fit to the transparency signal and subtract the intrinsic values  $\Omega_m$  and  $\Gamma_m$ . The remaining contributions to the resonance frequency and linewidth  $\delta\Omega_m$  and  $\Gamma_{\text{opt}}$ , respectively, correspond to the optical spring and optical damping by the microwave fields.

The result, shown in Fig. 3e, f, is quite surprising. Even though the optomechanical pump field is blue-detuned to all cavity resonances  $\omega_0$ ,  $\omega_s$ , and  $\omega_i$ , we observe dynamical backaction with characteristics resembling red-sideband pumping in linear optomechanical systems. Most strikingly, we find a positive optical damping, which is usually a clear signature for red-sideband physics and the basis for sideband cooling of the mechanical mode<sup>4</sup>. We use a linearized, optomechanical multi-tone Kerr cavity model, and implement the hierarchy from the experiment  $\alpha_d \gg \gamma_{\mp} \gg \langle \hat{a} \rangle$  to reveal which interactions are responsible for the observed behavior, cf. Supplementary Notes 8–10. The resulting effective mechanical susceptibility

$$\chi_0^{\text{eff}}(\Omega) = \frac{1}{\frac{\Gamma_m}{2} + i(\Omega - \Omega_m) + \Sigma_{\text{fw}}(\Omega_m)} \quad (9)$$

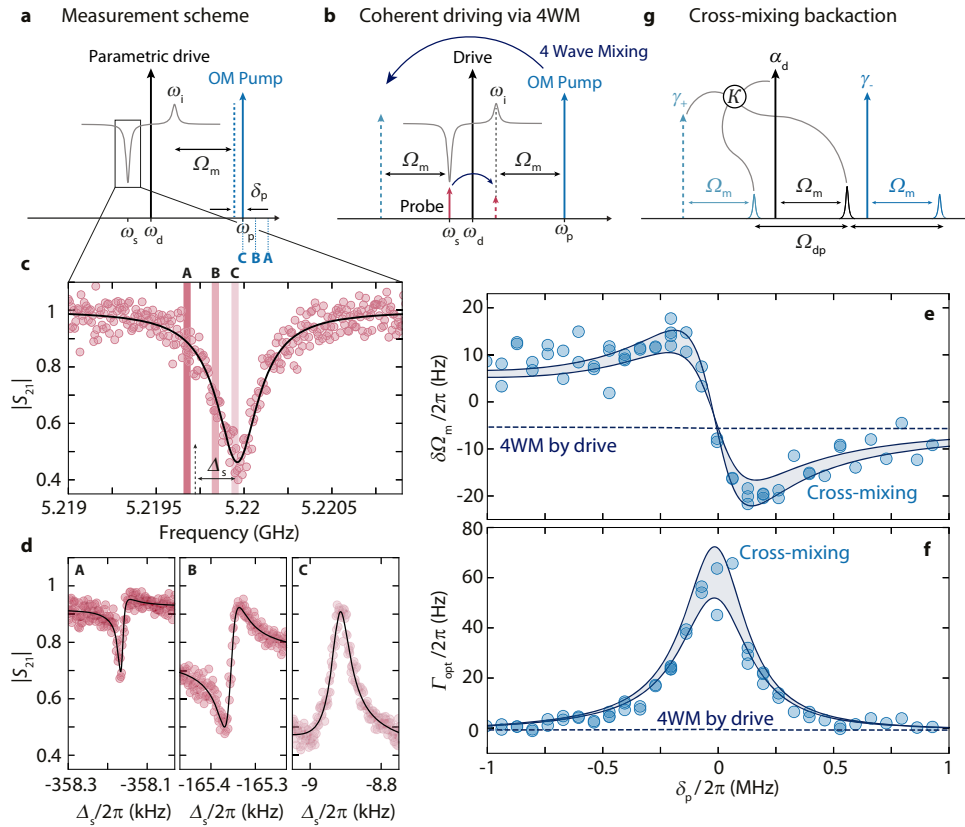


**Fig. 3 Four-wave OMIT and four-wave backaction for optomechanical blue-sideband pumping of the idler quasi-mode.** **a** Experimental protocol. The SQUID cavity is prepared in the quasi-mode state by a strong parametric drive (PD). In addition, an optomechanical (OM) pump tone is applied on the blue sideband of the idler resonance (IR)  $\omega_p = \omega_i + \Omega_m + \delta_p$ . Finally, we use a weak probe tone around the signal resonance (SR) to detect optomechanically induced transparency. We repeat this scheme for varying detunings  $\delta_p$ . **b** explains how this protocol to the first order leads to coherent driving of the mechanical oscillator. By PD-induced intracavity 4WM, the OM pump (probe tone) gets an idler field on the opposite side of the drive, which has the right detuning to the probe tone (pump)  $\sim \Omega_m$  to coherently drive the mechanical oscillator. **c** shows the signal resonance transmission  $S_{21}$  measured with the weak probe field (OM pump off). Circles are data, line is a fit. Vertical bars labeled with A, B, and C indicate zoom regions for the corresponding panels shown in **c** and  $\Delta_s = \omega - \omega_s$  denotes the detuning between probe field and SR. **d** Probe tone response (OM pump on) in three narrow-frequency windows around  $\omega \approx 2\omega_d - \omega_p + \Omega_m$  for three different pump detunings  $\delta_p$ , cf. panel **a**. Note that the frequency difference between OM pump and probe field is  $\Omega \approx \Omega_m - 2\Omega_{dp}$ , which implies that when the pump-field frequency is reduced, the probe-field frequency is increasing. Each probe-tone response displays a narrow-band resonance, indicating optomechanically induced transparency (OMIT) via excitation of the mechanical oscillator. For each  $\delta_p$ , we fit the OMIT response (lines in **c**) and extract the effective mechanical resonance frequency  $\Omega_{\text{eff}} = \Omega_m + \delta\Omega_m$  and the effective mechanical linewidth  $\Gamma_{\text{eff}} = \Gamma_m + \Gamma_{\text{opt}}$ . The contributions  $\delta\Omega_m$  and  $\Gamma_{\text{opt}}$ , induced by dynamical backaction of all intracavity fields, are plotted in panels **e** and **f** as circles vs  $\delta_p$ . The result of analytical calculations is shown as two solid lines with shaded area, where the range described by the lines captures uncertainties in the device parameters, cf. Supplementary Note 11. The dashed line shows the result of equivalent calculations without cross-mixing (nondegenerate 4WM) terms. **g** illustrates schematically one four-wave cross-mixing term that leads to the observed dynamical backaction. Hereby, two mechanical sidebands with frequency difference  $\Omega_{dp} = \omega_d - \omega_p$  and both, the PD and the OM pump, contribute to the interaction. For the data in **c-f**,  $B_{\parallel} = 21$  mT,  $g_0 = 2\pi \cdot 1.75$  kHz, and  $n_d \approx 69 \pm 11$ .

has still the same form as for a standard optomechanical system, and all the 4WM contributions can be captured in  $\mathcal{J}$ -factors in the dynamical four-wave backaction

$$\Sigma_{\text{fw}}(\Omega_m) = \sum_{j=-,\alpha,+} |g_j|^2 [\chi_{g,j} \mathcal{J}_j - \bar{\chi}_{g,j} \bar{\mathcal{J}}_j] \quad (10)$$

with  $g_- = \gamma_- g_0$ ,  $g_+ = \gamma_+ g_0$ ,  $\chi_{g,-} = \chi_g(\Omega_m)$ ,  $\chi_{g,\alpha} = \chi_g(\Omega_m + \Omega_{dp})$  and  $\chi_{g,+} = \chi_g(\Omega_m + 2\Omega_{dp})$ . Closed-form expressions for the  $\mathcal{J}$  are given in Supplementary Note 9. We identify nondegenerate four-wave mixing terms in the  $\mathcal{J}$ -factors as the dominant origin of the observed backaction. These terms have contributions from the drive field  $\alpha_d$ , from one of the  $\gamma_{\pm}$  fields, and couple any two distinct mechanical sidebands that have the frequency difference  $\pm\Omega_{dp}$ , cf. Fig. 3g for a schematic of one of these terms. Hence, these terms correspond to intracavity cross-mixing based on  $\alpha_d$  and  $\gamma_{\pm}$  fields. Using independently determined system

parameters, we find excellent agreement between the experimental data and the analytical model when we take these cross-mixing terms into account, cf. solid lines in Fig. 3e, f. If we take only the degenerate 4WM terms into account, which are induced by the presence of  $\alpha_d$ , we find a small and nearly constant backaction for all  $\delta_p$ , cf. dashed lines.

**Blue-detuned four-wave cooling close to the groundstate.**

Positive optical damping is commonly related to cooling of the mechanical mode. Therefore, the blue-detuned pumping scheme described in Fig. 3 seems feasible to be utilized as a counterintuitive, yet innovative, method to eliminate the residual thermal excitations in the mechanical resonator. It is a particularly exciting option here, as blue-detuned pumping offers the opportunity to evade the Kerr bistability of the cavity,

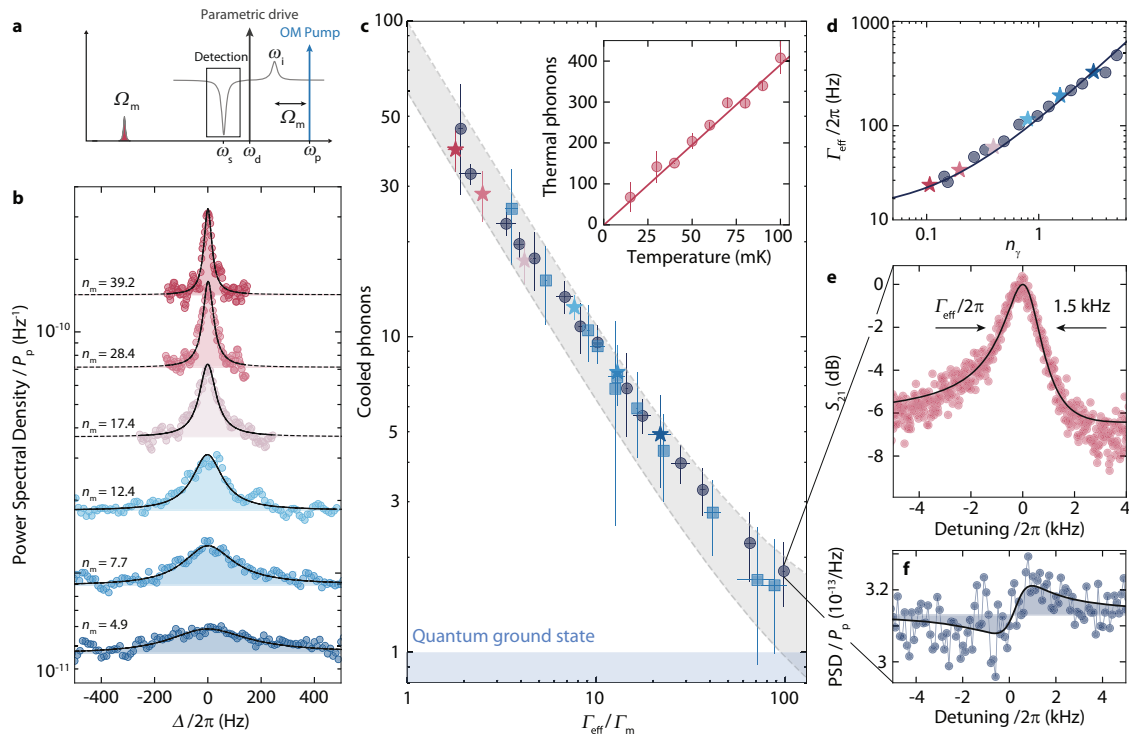


**Fig. 4 Blue-detuned four-wave-cooling of a mechanical oscillator close to its quantum groundstate.** **a** Schematic representation of the experiment. A parametric drive is used to activate the quasi-mode state and an optomechanical (OM) pump is sent to the blue sideband of the idler resonance  $\omega_p \approx \omega_i + \Omega_m$ . The signal resonance output power spectral density is measured using a spectrum analyzer around  $\omega = \omega_p + 2\Omega_{dp} + \Omega_m \approx \omega_s$ . **b** Power spectral densities normalized to the optomechanical pump input power  $P_p$  for various pump powers. Frequency axis is given with respect to  $\omega = \omega_p + 2\Omega_{dp} + \Omega_m$ . With increasing pump power, the linewidth of the upconverted mechanical noise spectrum is increasing, indicating four-wave dynamical backaction damping. Simultaneously, the area of the normalized signal decreases, indicating cooling of the mode. From fits (lines and shaded areas) to the data (points), we determine the resulting phonon occupation  $n_m$ . In **c**, we show the cooled phonon number vs  $\Gamma_{\text{eff}}/\Gamma_m$  in a collection of several different datasets. Intracavity drive photon numbers vary between different points in the range  $30 < n_d < 110$ . Circles correspond to data from measurements at operation point I and squares to data from operation point II. Stars show the points that correspond to the data shown in **b**, taken at operation point I. All measurements have been taken at  $B_{\parallel} = 25$  mT. The inset shows the result of a thermal calibration measurement, indicating that the mechanical oscillator mode equilibrates with the fridge base temperature and the residual thermal occupation at  $T_b = 15$  mK is  $n_m^{\text{th}} \approx 70 - 90$ . Dashed lines and shaded area display the theoretically calculated range of four-wave-cooled phonon occupation, taking into account a possible range of  $60 \leq n_m^{\text{th}} \leq 100$  and  $45 \leq n_d \leq 90$ . Parametric amplification of cavity quantum noise limits the minimally achievable phonon occupation in our parameter regime to  $n_m^{\text{lim}} \sim 0.6$ . For the highest powers, we exceed this theoretical limit by only a factor  $\sim 3$ . **d** shows the effective effective mechanical linewidth vs intracavity sideband photon number  $n_\gamma = |\gamma_-|^2 + |\gamma_+|^2$  for points from **c**, which have nearly constant  $n_d \approx 87 \pm 11$ , demonstrating that we achieve significant cooling with a small number of photons. The line corresponds to theory with  $\Gamma_m = 2\pi \cdot 15$  Hz. **e** shows an OMIT scan at the point of largest cooling  $\Gamma_{\text{eff}}$  with an effective linewidth  $\Gamma_{\text{eff}} \approx 2\pi \cdot 1.5$  kHz, which corresponds to an effective four-wave cooperativity of  $C_{\text{fw}} \gtrsim 100$ . **f** shows the corresponding power-spectral density in units of quanta, displaying an asymmetric-noise lineshape due to a small, but finite effective temperature of the cavity by amplified quantum noise. Error bars in **c** consider uncertainties in the fitting procedure and in the bare mechanical linewidth, for details see Supplementary Note 14.

which becomes more relevant with increasing sideband-pump power.

To characterize the mechanical mode temperature, we detect the upconverted thermal displacement fluctuations in the signal resonance output field with a spectrum analyzer. For this measurement, the SQUID cavity in the quasi-mode state is pumped with an optomechanical tone on the blue sideband of the idler mode. Using a probe tone, we then measure the signal-mode response  $S_{21}$  in a wide-frequency range and the OMIT response in a narrow range. Finally, we detect the output spectrum in the same frequency window where the OMIT is observed, cf. also Fig. 4a. A collection of spectra for varying optomechanical pump power  $P_p$  is presented in Fig. 4b. From a careful analysis of the combined datasets, cf. Supplementary Notes 8–13, the equilibrium phonon occupation of the mechanical oscillator as well as the phonon occupation resulting from four-wave cooling can be inferred.

The mechanical oscillator is well thermalized to the mixing chamber base temperature and its residual phonon occupation at the lowest operation temperature  $T_b = 15$  mK is about  $n_m^{\text{th}} \approx 70 - 90$  phonons, cf. inset of Fig. 4c. With increasing optical damping caused by the blue-detuned pump tone, we observe a corresponding reduction of the initial thermal occupation and the cooling factor is determined by  $\Gamma_{\text{opt}}$ , very similar to the usual optomechanical sideband cooling. The observed four-wave cooling is also very robust with respect to pump and drive strengths and we achieve at both flux bias operation points a final four-wave-cooled occupation extremely close to the quantum groundstate  $n_m \sim 1.6$ . Due to the high single-photon coupling rates, it requires only a small amount of effective sideband photons  $n_\gamma = |\gamma_-|^2 + |\gamma_+|^2 \lesssim 10$  to achieve these low occupations. A summary of these findings is presented in Fig. 4c–f.

The fact that we use strongly driven Kerr quasi-modes as cold bath, however, modifies the minimally achievable occupation.

Due to Josephson parametric amplification of quantum noise in the quasi-mode state, the cavity will acquire an effective temperature, even if the bare cavity is in the quantum groundstate. This drive-induced cavity heating defines the cooling limit for the mechanical resonator. In the state we are operating here, the Josephson gain is small and the effective thermal occupation of the cavity is still considerably below 1. We estimate the current cooling limit due to amplified quantum noise to be  $\sim 0.6$ , where the exact value depends on the drive strength  $n_d$  and on the bias-flux operation point. With higher bias-flux stability, the cavity could be stabilized at a point where the Josephson gain is small enough to enable  $n_m^{\text{lim}} < 0.3$ .

Achieving the lowest occupation in the current device requires a careful balancing of drive and pump strength, and for the highest pump powers, we observe the onset of additional cavity shifts and line broadening, possibly related to drive depletion or higher-order nonlinear effects. With slightly optimized device parameters regarding  $\mathcal{K}$  and  $g_0$ , we should therefore be able to cool to  $n_m < 1$ . We emphasize though, that the blue-detuned cooling scheme allowed to achieve a significantly lower phonon occupation than signal-mode red-sideband pumping. With a pump on the red signal-mode sideband, a second cavity-bifurcation instability occurs at moderately high pump powers, as the red-sideband pump is attracting the cavity, while the blue-detuned pump is repelling it. The related jump to a high-amplitude state with a different signal resonance frequency, prevents us from cooling below  $n_m^{\text{red}} \sim 5$ . The corresponding red-sideband cooling data and analysis can be found in Supplementary Note 16.

## Conclusions

The results we presented here demonstrate clearly that the young field of flux-mediated optomechanics is quickly advancing toward an exciting and competitive optomechanical platform, which intrinsically allows for novel ways of manipulating mechanical motion. Our device provides a large single-photon coupling rate of up to  $g_0 = 2\pi \cdot 3.6$  kHz and achieves large cooperativities of up to  $C_{\text{fw}} > 100$  for small numbers of intracavity photons. By using strong parametric driving, we show how the intrinsic Josephson-based Kerr nonlinearity can be utilized as a resource for improved sideband resolution, for the generation of frequency stability by an internal feedback-locking scheme, and for the implementation of a four-wave mixing-based phonon-control scheme. In combination, these properties enabled us to use four-wave cooling in a Kerr cavity to prepare a MHz mechanical nanobeam resonator close to its quantum groundstate. While implemented here using a SQUID cavity, we note that both of these techniques could be applied to any system with a Kerr nonlinearity, also in the case where flux-mediated optomechanics is not employed.

Future device improvements can be achieved by reducing the SQUID loop inductance further in order to increase the flux responsivity and the single-photon coupling rate. One order of magnitude is a feasible goal in this direction, as related platforms have already demonstrated such high responsivities<sup>16,17</sup>. This improvement alone would bring the device to a cooperativity of  $10^4$  and to the onset of the strong-coupling regime with  $g \sim 2\pi \cdot 150$  kHz  $\sim \kappa/2$ . With increased in-plane fields, up to  $\sim 1$  T using, e.g., niobium or granular aluminum, those numbers could be improved by another order of magnitude.

In the current device, however, the main limiting factor that prevented us from achieving higher coupling rates and from cooling the mechanical oscillator into the groundstate was external flux noise coupling into the SQUID in large in-plane fields. We suspect that the origin of this flux noise is in the vector-magnet leads and the used current sources, respectively, or in

parasitic out-of-plane components that lead to flux instabilities, vortex avalanches, and microwave-triggered vortex motion in proximity to the SQUID. Flux noise in the leads and current sources could potentially be reduced by using a superconducting magnet in persistent current mode. Although our current setup can locally cancel parasitic out-of-plane fields, it cannot do so over the complete chip simultaneously due to the geometry of the small coil. A global compensation might be necessary, however, to completely avoid any flux instabilities arising from the out-of-plane fields, which can cause flux fluctuations also in large distances from their occurrence. The demands for flux-noise suppression, however, are significantly relaxed by the presented stabilization mechanism.

Using intrinsic Kerr nonlinearities as a resource in optomechanical systems has just begun. Further interesting directions in Kerr optomechanics might involve intracavity squeezing, intracavity Josephson parametric amplification<sup>39</sup>, intracavity cat-state generation<sup>40</sup>, groundstate cooling in the sideband-unresolved regime, or enhanced quantum transduction<sup>31</sup>. Significantly larger Kerr nonlinearities than the ones presented here, implemented in superconducting transmon qubits, have also been discussed recently for mechanical quantum-state preparation<sup>24,41,42</sup>. Similar schemes investigating and exploiting the Kerr nonlinearity of SQUID circuits could furthermore be implemented naturally in the platform of photon-pressure-coupled circuits<sup>43–45</sup>. Therefore, we believe that Kerr optomechanics will constitute an extremely versatile and exciting platform for the preparation and investigation of mechanical quantum states and for optomechanical quantum technologies.

## Methods

**Sample fabrication.** The first fabrication step is the patterning and deposition of the constriction-type Josephson junctions (cJJs). The resist patterning is done using electron beam lithography (EBL), followed by the DC magnetron sputtering of a 15-nm-thick layer of Al (1% Si) and liftoff in Anisole. In this first layer, we structure the narrow constrictions ( $\sim 100$  nm-long and  $\sim 50$  nm wide) together with two  $\sim 1 \mu\text{m}^2$  large contact pads at each junction for a good galvanic contact to the rest of the circuit deposited in the second step. In the second step, all the remaining circuit is patterned using EBL again and an  $\sim 70$ -nm-thick Al (1% Si) layer is deposited, followed again by liftoff in Anisole. Directly before the sputter deposition, an in situ Ar-ion milling step is performed to remove the native oxide layer on top of the cJJ contact pads in order to achieve a low-loss galvanic contact between the layers. After testing the samples at this stage in a dilution refrigerator, we apply another well-timed Ar-ion milling process to the SQUID (the rest of the sample is covered in EBL-patterned resist) to finetune/reduce the critical currents of the junctions in order to achieve a good balance between screening parameter  $\beta_L$  and the Kerr nonlinearity  $\mathcal{K}$ . The mechanical oscillator part of the SQUID loop is released in the last major fabrication step by EBL patterning a release window next to the SQUID loop into a fourth resist layer and exposing the sample to an isotropic reactive-ion etching process in  $\text{SF}_6$  plasma. The remaining resist after this step is removed by  $\text{O}_2$  plasma ashing. Finally, the sample is glued and wirebonded into a microwave printed-circuit board and mounted into the magnet body as shown in Fig. 1 A, more detailed description and a schematic of the fabrication process are given in Supplementary Note 1.

**Experimental setup.** Figure 1 shows photographs of the sample mounted on the PCB and fixed in the vector magnet bobbin. The two large parallel coils on each side of the sample are wound from a single wire (niobium–titanium in copper–nickel matrix) and in the same orientation and therefore form a Helmholtz-like split coil (the distance between the coils is slightly larger than their effective radius), which creates a nearly homogeneous in-plane magnetic field at the location of the device. The coil has approximately 2000 windings of superconducting wire on each side. From the coil geometry and the number of windings, we estimate the current-to-field conversion factor to be 70 mT/A. On the backside of the sample/PCB platform within the magnet bobbin is a second small coil mounted for providing the out-of-plane magnetic field used to tune the SQUID flux-bias point. This out-of-plane coil can also be used to compensate for a parasitic out-of-plane component of the in-plane field due to misalignments of the sample/PCB with respect to the in-plane field axis (estimated to be around  $2^\circ$ – $3^\circ$  from the SQUID flux response). For in-plane fields  $B_{\parallel} \lesssim 25$  mT, however, the compensation is not yet critical. For larger in-plane fields, vortices start to penetrate the film and there is a dramatic reduction in the cavity quality factor observable. The out-of-plane coil has approximately 400 turns of superconducting wire and to a conversion factor of 1 mT/A. The superconducting wires leading to each of the



coils from the 3-K plate are twisted in pairs, in order to reduce the amount of captured flux noise. Furthermore, since the critical temperature of the wire is about  $\sim 12$  K, the wires can go unbroken until the 3-K stage. Above this plate, the wires are no longer superconducting and therefore a transition to normal conducting wires is required. For this, we connected each of the superconducting in-plane coil wires to 9 wires of a 24-line copper loom provided by Bluefors and each of the out-of-plane coil wires to 3 wires of the loom. From the 3-K stage until room temperature the current flows in parallel through the respective loom wires, decreasing the additional heat load on the plate. With this approach, we are able to send  $I_{||} \sim 0.5$  A through the in-plane coil without any considerable heat added to any of the plates and maintaining the fridge base temperature. At room temperature, we are left with 4 cables, two for each coil, which are used with individual directed current (DC) sources to independently generate the magnetic fields.

The experiments reported in this paper were performed in a dilution refrigerator with a base temperature  $T_b \approx 15$  mK. Within the outer vacuum can of the system, a mu-metal shield is installed to provide basic magnetic shielding for the whole sample space from the 3 K plate to the mK plate. A schematic diagram of the experimental setup and of the external measurement configuration used in the reported experiments can be seen in Supplementary Note 2. The PCB, onto which the fabricated sample is glued and wirebonded, is mounted into the magnet casing and connected to two coaxial lines. The complete configuration, including the vector magnet, is placed in a magnetic cryoperm shield. Since the optomechanical circuit that we present in this paper is designed in a side-coupled geometry, the input and output signals were sent/received through separate coaxial lines in order to measure the transmission spectrum of the feedline to which the system is coupled. The input line is heavily attenuated in order to balance the thermal radiation from the line to the base temperature of the fridge and the output line contains a cryogenic HEMT (high-electron-mobility transistor) amplifier working in a range from 4 to 8 GHz and two isolators to block the thermal radiation from the HEMT to reach the sample. Outside of the refrigerator, we used a single-measurement scheme for all the different experiments. The VNA was used to measure the response spectrum  $S_{21}$  of the electromechanical system, one microwave generator sends a coherent signal at  $\omega_d$  as parametric drive for the SQUID cavity and the second microwave generator sends a tone at  $\omega_p$  as optomechanical pump for the parametrically driven cavity. Finally, a spectrum analyzer was used to record the output power spectrum around the cavity resonance. For all experiments, the microwave sources and vector-network analyzers (VNA) as well as the spectrum analyzer used a single reference clock of one of the devices.

## Data availability

All data and processing scripts of the results presented in this paper, including those in the Supplementary Information, are available on Zenodo with the identifier <https://doi.org/10.5281/zenodo.5647568>. Supplementary Information for this paper, which includes additional references<sup>46–50</sup>, is available under <https://doi.org/10.1038/s42005-022-00808-3>.

Received: 2 August 2021; Accepted: 17 December 2021;

Published online: 02 February 2022

## References

- Aspelmeyer, M., Kippenberg, T. J. & Marquardt, F. Cavity optomechanics. *Rev. Mod. Phys.* **86**, 1391 (2014).
- Teufel, J. D., Donner, T., Castellanos-Beltran, M. A., Harlow, J. W. & Lehnert, K. W. Nanomechanical motion measured with an imprecision below that at the standard quantum limit. *Nat. Nanotechnol.* **4**, 820–823 (2009).
- Mason, D., Chen, J., Rossi, M., Tsaturyan, Y. & Schliesser, A. Continuous force and displacement measurement below the standard quantum limit. *Nat. Phys.* **15**, 745–749 (2019).
- Teufel, J. D. et al. Sideband-cooling of micromechanical motion to the quantum ground state. *Nature* **475**, 359–363 (2011).
- Chan, J. et al. Laser cooling of a nanomechanical oscillator into its quantum ground state. *Nature* **478**, 89–92 (2011).
- Wollman, E. E. et al. Quantum squeezing of motion in a mechanical resonator. *Science* **349**, 952–955 (2015).
- Riedinger, R. et al. Non-classical correlations between single photons and phonons from a mechanical oscillator. *Nature* **530**, 313–316 (2016).
- Reed, A. P. et al. Faithful conversion of propagating quantum information to mechanical motion. *Nat. Phys.* **13**, 1163–1167 (2017).
- Ma, X., Viennot, J. J., Kotler, S., Teufel, J. D. & Lehnert, K. W. Non-classical energy squeezing of a macroscopic mechanical oscillator. *Nat. Phys.* **17**, 322–326 (2021).
- Riedinger, R. et al. Remote quantum entanglement between two micromechanical oscillators. *Nature* **556**, 473–477 (2018).
- Ockeloen-Korppi, C. F. et al. Stabilized entanglement of massive mechanical oscillators. *Nature* **556**, 478–482 (2018).
- Xu, H., Mason, D., Jiang, L. & Harris, J. G. E. Topological energy transfer in an optomechanical system with exceptional points. *Nature* **537**, 80–83 (2016).
- Andrews, R. W. et al. Bidirectional and efficient conversion between microwave and optical light. *Nat. Phys.* **10**, 321–326 (2014).
- Forsch, M. et al. Microwave-to-optics conversion using a mechanical oscillator in its quantum ground state. *Nat. Phys.* **16**, 69–74 (2020).
- Rodrigues, I. C., Bothner, D. & Steele, G. A. Coupling microwave photons to a mechanical resonator using quantum interference. *Nat. Commun.* **10**, 5359 (2019).
- Zoepfl, D., Juan, M. L., Schneider, C. M. F. & Kirchmair, G. Single-photon cooling in microwave magnetomechanics. *Phys. Rev. Lett.* **125**, 023601 (2020).
- Schmidt, P. et al. Sideband-resolved resonator electromechanics based on a nonlinear Josephson inductance probed on the single-photon level. *Commun. Phys.* **3**, 233 (2020).
- Bera, T., Majumder, S., Sahu, S. K. & Singh, V. Large flux-mediated coupling in hybrid electromechanical system with a transmon qubit. *Commun. Phys.* **4**, 12 (2021).
- Xue, F. et al. Controllable coupling between flux qubit and nanomechanical resonator by magnetic field. *New J. Phys.* **9**, 35 (2007).
- Nation, P. D., Blencowe, M. P. & Buks, E. Quantum analysis of a nonlinear microwave cavity-embedded dc SQUID displacement detector. *Phys. Rev. B* **78**, 104516 (2008).
- Shevchuk, O., Steele, G. A. & Blanter, Ya. M. Strong and tunable couplings in flux-mediated optomechanics. *Phys. Rev. B* **96**, 014508 (2017).
- Nunnenkamp, A., Børkje, K. & Girvin, S. M. Single-photon optomechanics. *Phys. Rev. Lett.* **107**, 063602 (2011).
- Rabl, P. Photon blockade effect in optomechanical systems. *Phys. Rev. Lett.* **107**, 063601 (2011).
- Kounalakis, M., Blanter, Ya. M. & Steele, G. A. Flux-mediated optomechanics with a transmon qubit in the single-photon ultrastrong-coupling regime. *Phys. Rev. Res.* **2**, 023335 (2020).
- Fani Sanj, F., Rodrigues, I. C., Bothner, D. & Steele, G. A. Level attraction and idler resonance in a strongly driven Josephson cavity. *Phys. Rev. Res.* **3**, 043111 (2021).
- Kumar, T., Bhattacharjee, A. B. & Man, M. Dynamics of a movable micromirror in a nonlinear optical cavity. *Phys. Rev. A* **81**, 013835 (2010).
- Mikkelsen, M., Fogarty, T., Twamley, J. & Busch, T. Optomechanics with a position-modulated Kerr-type nonlinear coupling. *Phys. Rev. A* **96**, 043832 (2017).
- Asjad, M., Abari, N. E., Zippilli, S. & Vitali, D. Optomechanical cooling with intracavity squeezed light. *Opt. Express* **27**, 32427–32444 (2019).
- Gan, J.-H., Liu, Y.-C., Lu, C., Wang, X., Tey, M.-K. & You, L. Intracavity-squeezed optomechanical cooling. *Laser Photonics Rev.* **13**, 1900120 (2019).
- Qiu, L. et al. Floquet dynamics in the quantum measurement of mechanical motion. *Phys. Rev. A* **100**, 053852 (2019).
- Lau, H.-K. & Clerk, A. A. Ground-state cooling and high-fidelity quantum transduction via parametrically driven bad-cavity optomechanics. *Phys. Rev. Lett.* **124**, 103602 (2020).
- Norte, R. A., Forsch, M., Wallucks, A., Marinković, I. & Gröblacher, S. Platform for measurements of the Casimir force between two superconductors. *Phys. Rev. Lett.* **121**, 030405 (2018).
- Drummond, P. D. & Walls, D. F. Quantum theory of optical bistability. I. Nonlinear polarisability model. *J. Phys. A Math. Gen.* **13**, 725 (1980).
- Khandekar, C., Lin, Z. & Rodriguez, A. W. Thermal radiation from optically driven Kerr ( $\chi^{(3)}$ ) photonic cavities. *Appl. Phys. Lett.* **106**, 151109 (2015).
- Huber, J. S. et al. Spectral evidence of squeezing of a weakly damped driven nanomechanical mode. *Phys. Rev. X* **10**, 021066 (2020).
- Schliesser, A., Del'Haye, P., Nooshi, N., Vahala, K. J. & Kippenberg, T. J. Radiation pressure cooling of a micromechanical oscillator using dynamical backaction. *Phys. Rev. Lett.* **97**, 243905 (2006).
- Teufel, J. D., Harlow, J. W., Regal, C. A. & Lehnert, K. W. Dynamical backaction of microwave fields on a nanomechanical oscillator. *Phys. Rev. Lett.* **101**, 197203 (2008).
- Weis, S. et al. Optomechanically induced transparency. *Science* **330**, 1520–1523 (2010).
- Castellanos-Beltran, M. A., Irwin, K. D., Hilton, G. C., Vale, L. R. & Lehnert, K. W. Amplification and squeezing of quantum noise with a tunable Josephson metamaterial. *Nat. Phys.* **4**, 929–931 (2008).
- Leghtas, Z. et al. Confining the state of light to a quantum manifold by engineered two-photon loss. *Science* **347**, 853–857 (2015).
- Khosla, K. E., Vanner, M. R., Ares, N. & Laird, E. A. Displacement electromechanics: how to detect quantum interference in a nanomechanical resonator. *Phys. Rev. X* **8**, 021052 (2018).
- Kounalakis, M., Blanter, Y. M. & Steele, G. A. Synthesizing multi-phonon quantum superposition states using flux-mediated three-body interactions with superconducting qubits. *NPJ Quantum Inf.* **5**, 100 (2019).
- Eichler, C. & Petta, J. R. Realizing a circuit analog of an optomechanical system with longitudinally coupled superconducting resonators. *Phys. Rev. Lett.* **120**, 227702 (2018).

44. Bothner, D., Rodrigues, I. C. & Steele, G. A. Photon-pressure strong coupling between two superconducting circuits. *Nat. Phys.* **17**, 85–91 (2021).
45. Rodrigues, I. C., Bothner, D. & Steele, G. A. Cooling photon-pressure circuits into the quantum regime. *Sci. Adv.* **7**, eabg6653 (2021).
46. Igreja, R. & Dias, C. J. Analytical evaluation of the interdigital electrodes capacitance for a multi-layered structure. *Sens. Actuators A* **112**, 291–301 (2004).
47. Levenson-Falk, E. M., Vijay, R. & Siddiqi, I. Nonlinear microwave response of aluminum weak-link Josephson oscillators. *Appl. Phys. Lett.* **98**, 123115 (2011).
48. Pogorzalek, S. et al. Hysteretic flux response and nondegenerate gain of flux-driven Josephson parametric amplifiers. *Phys. Rev. Appl.* **8**, 024012 (2017).
49. Capelle, T. et al. Probing a two-level system bath via the frequency shift of an off-resonantly driven cavity. *Phys. Rev. Appl.* **13**, 034022 (2020).
50. Brock, B. L., Blencowe, M. P. & Rimberg, A. J. Frequency fluctuations in tunable and nonlinear microwave cavities. *Phys. Rev. Appl.* **14**, 054026 (2020).

### Acknowledgements

This research was supported by the Netherlands Organisation for Scientific Research (NWO) in the Innovational Research Incentives Scheme—VIDI, project 680-47-526. This project has received funding from the European Research Council (ERC) under the European Union's Horizon 2020 research and innovation programme (grant agreement No 681476—QOMD) and from the European Union's Horizon 2020 research and innovation programme under grant agreement No 732894—HOT. The authors thank Ronald Bode for the construction of the 2D vector magnet, Olaf Benningshof and Raymond Schouten for useful discussions, and D. Koelle and R. Kleiner for providing the High-Finesse current source used to power the in-plane magnet.

### Author contributions

All authors conceived the experiment. DB and ICR designed the device, performed the experiments, and analyzed the data. ICR fabricated the device. DB developed the theoretical treatment. DB and ICR edited the paper with input from GAS. All authors discussed the results and the paper. GAS supervised the project.

### Competing interests

The authors declare no competing interests.

### Additional information

**Supplementary information** The online version contains supplementary material available at <https://doi.org/10.1038/s42005-022-00808-3>.

**Correspondence** and requests for materials should be addressed to Daniel Bothner or Gary A. Steele.

**Peer review information** Communications Physics thanks Atsushi Noguchi and the other, anonymous, reviewer(s) for their contribution to the peer review of this work. Peer reviewer reports are available.

**Reprints and permission information** is available at <http://www.nature.com/reprints>

**Publisher's note** Springer Nature remains neutral with regard to jurisdictional claims in published maps and institutional affiliations.



**Open Access** This article is licensed under a Creative Commons Attribution 4.0 International License, which permits use, sharing, adaptation, distribution and reproduction in any medium or format, as long as you give appropriate credit to the original author(s) and the source, provide a link to the Creative Commons license, and indicate if changes were made. The images or other third party material in this article are included in the article's Creative Commons license, unless indicated otherwise in a credit line to the material. If material is not included in the article's Creative Commons license and your intended use is not permitted by statutory regulation or exceeds the permitted use, you will need to obtain permission directly from the copyright holder. To view a copy of this license, visit <http://creativecommons.org/licenses/by/4.0/>.

© The Author(s) 2022